A Stochastic Model for the Spatial Structure of Annular Patterns of Variability and the North Atlantic Oscillation

EDWIN P. GERBER

Program in Applied and Computational Mathematics, Princeton University, Princeton, New Jersey

GEOFFREY K. VALLIS

GFDL, Princeton University, Princeton, New Jersey

(Manuscript received 7 April 2004, in final form 7 October 2004)

ABSTRACT

Meridional dipoles of zonal wind and geopotential height are found extensively in empirical orthogonal function (EOF) analysis and single-point correlation maps of observations and models. Notable examples are the North Atlantic Oscillation and the so-called annular modes (or the Arctic Oscillation). Minimal stochastic models are developed to explain the origin of such structure. In particular, highly idealized, analytic, purely stochastic models of the barotropic, zonally averaged zonal wind and of the zonally averaged surface pressure are constructed, and it is found that the meridional dipole pattern is a natural consequence of the conservation of zonal momentum and mass by fluid motions. Extension of the one-dimensional zonal wind model to two-dimensional flow illustrates the manner in which a local meridional dipole structure may become zonally elongated in EOF analysis, producing a zonally uniform EOF even when the dynamics is not particularly zonally coherent on hemispheric length scales. The analytic system then provides a context for understanding the existence of zonally uniform patterns in models where there are no zonally coherent motions. It is also shown how zonally asymmetric dynamics can give rise to structures resembling the North Atlantic Oscillation. Both the one- and two-dimensional results are manifestations of the same principle: given a stochastic system with a simple red spectrum in which correlations between points in space (or time) decay as the separation between them increases, EOF analysis will typically produce the gravest mode allowed by the system's constraints. Thus, grave dipole patterns can be robustly expected to arise in the statistical analysis of a model or observations, regardless of the presence or otherwise of a dynamical mode.

1. Introduction

A problem of considerable interest is the proper characterization of intraseasonal (sometimes called low frequency, here meaning time scales between about 10 and 100 days) variability in the extratropics. In particular, many analyses of the spatial structure of such variability result in meridional dipole patterns—they appear in empirical orthogonal function (EOF) analysis and single-point correlation maps of observations of both the geopotential height and zonal wind (e.g., Wallace and Gutzler 1981; Barnston and Livezey 1987) and in models (e.g., Limpasuvan and Hartmann 2000; Cash et al. 2002). The zonal structure of the EOFs is generally more uniform, especially in the Southern Hemisphere, while the correlation patterns are more local. Interpreting such patterns has been problematic, for they do not clearly differentiate between a hemispheric-scale dynamical mode of oscillation (Thompson and Wallace 2000) and dynamics that are more regional in nature (Ambaum et al. 2001). Wallace (2000) provides a summary of the issues. For example, the first EOF of the low-passed (>10 day period) surface pressure in the Southern Hemisphere is almost zonally uniform, and might be called an annular mode. In the Northern Hemisphere, the corresponding EOF is more regional and resembles a pattern of variability traditionally known as the North Atlantic Oscillation (NAO), although it is now known (essentially by definition) as the Northern Annular Mode or the Arctic Oscillation (AO). As Wallace (2000) points out, the

Corresponding author address: Dr. Geoffrey K. Vallis, AOS Program, Princeton University, P.O. Box CN710, Sayre Hall, Princeton, NJ 08544-0710.
E-mail: gkv@princeton.edu

name North Atlantic Oscillation implies regional dynamics, perhaps even a role for the ocean, whereas referring to it as an annular mode or Arctic Oscillation implies more hemispheric dynamics. In this paper our goal is to clarify what underlying processes give rise to such patterns and to suggest a simple model, perhaps the simplest possible model, for them.

In Vallis et al. (2004, hereafter denoted V04), a barotropic model was employed to illustrate a mechanism for the generation of meridional dipole patterns. The authors found that robust annular mode–like and NAO-like patterns of variability could be generated with a simple midlatitude stirring. It was concluded that both the AO and NAO in their model were created by the same dynamics. It was further noted that the annular mode of their model did not necessarily indicate the presence of a zonally uniform dynamical mode, but rather reflected the fact that the same "meridional dipole forming mechanism" was acting at all longitudes. Drawing on these results, we develop a purely stochastic model for understanding the spatial structure of the single-point correlation maps and EOFs characterizing the NAO and AO.

EOF analysis allows one to represent a variable of interest in the most efficient set of orthogonal modes, using only the variable's covariance function as input. It further quantifies the variance represented by the modes, reflecting the importance of each in describing the covariance structure.[1] Stochastic models, that is, models of "random motions," have long been used to better understand EOF and correlation patterns. An understanding of the space of all potential motions can provide insight into the space of observed motions. Batchelor (1953) notes in his section 2.5 that the statistical stationarity of homogeneous turbulence necessitates the choice of trigonometric functions when seeking an orthogonal basis. North and Cahalan (1981) report a theorem by Obukhov (1947) that the EOFs of a statistically uniform random field on the sphere are the spherical harmonics. In both cases, the variance represented by each EOF is dependent on the decorrelation spectrum. If the field is "white" in space, the spectrum is flat; all modes are degenerate, explaining the same fraction of variance. When the field is "reddened" so that spatial correlations decay over a finite distance, the modes separate. If this reddening is simple so that covariance between two points decorrelates monotonically as the distance between them increases (e.g., exponential decay), the gravest mode allowed by the geometry of the system will be the top EOF, and the variance represented by each mode decreases with increasing wavenumber.

With idealized three-dimensional turbulence in a box with periodic boundaries and random motion on the sphere, symmetries in the system lead to the selection of the EOF basis. The extratropical atmosphere is more constrained than homogeneous turbulence, and we may wonder what the symmetries and constraints of the circulation imply for the selection of an EOF basis. In section 2 we present a one-dimensional model of the barotropic zonally averaged zonal wind, which suggests that the oft-observed meridional dipole pattern is a natural consequence of angular momentum conservation on a sphere, or zonal momentum conservation in a channel. We extend the model to two dimensions in section 3 to illustrate the potential for annular modes in a system with no zonally coherent motions. In section 4, we find that the addition of a relatively small degree of zonal inhomogeneity, that is, a storm track, localizes an annular mode–like pattern to a NAO-like pattern. We then discuss the relation between EOFs of zonal wind and of pressure in section 5. Differences are illustrated by two one-dimensional models of the zonally averaged surface pressure, where we find that the conservation of mass plays a similar role as the conservation of momentum in establishing the dipole pattern. From the outset, we seek to explain the observations from the V04 model, but believe the results have relevance to the AO and NAO of the atmosphere.

2. A one-dimensional model

a. Theory

We begin our discussion with the barotropic zonally averaged zonal wind. Our model is a stochastic process $M(\omega, y)$ designed to catalog all possible anomalies of the barotropic jet. The variable $y \in [0, 1]$ is our meridional coordinate, 0 being the equator and 1 the pole. Here ω marks the process in probability space: for each particular ω^*, $M(\omega^*, y)$ represents one realization of an anomalous zonally averaged barotropic wind profile. Sampling M is analogous to sampling the wind profile from a dynamically evolving model over time increments sufficiently long enough for the zonal anomalies to be independent of one another, say 10 days to a month.

We keep M as general as possible, but each realization should be in keeping with the basic physical properties of the atmospheric jet.

[1] For data on a finite grid, EOFs are the eigenvectors of the covariance matrix, whose ijth entry is the covariance between points i and j. The corresponding eigenvalues quantify the variance represented by each eigenvector. The generalization of EOF analysis to continuous functions is also known as a Karhunen–Loéve decomposition. [See von Storch and Zwiers (1999), chapter 13, for a complete discussion.]

1) The jet varies little in the Tropics.
2) The jet must vanish at the pole.
3) The fluid motions that generate the jet conserve zonal momentum.

Constraint 1 is motivated by V04, which suggests that NAO/AO variability arises from the eddy-driven component of the midlatitude jet with little variation at low latitudes. At the pole, geometry fixes the zonal wind at zero. Constraint 3 accounts for the fact that fluid motions, midlatitude eddies in particular, conserve momentum, and so can only reorganize momentum within the atmosphere; anomalous momentum convergence at one latitude must then be at the expense of momentum lost at another. We enforce this constraint by requiring that realizations of M have zero mean. We thus ignore variations of the density with latitude and approximate the hemisphere as a channel, but this does not qualitatively affect our conclusions. Likewise, one could view M as a model of the angular momentum, where the application to spherical geometry is more straightforward. The complete mathematical translation of the three constraints is then that M must satisfy

$$M(\omega, 0) = 0 \tag{2.1a}$$

$$M(\omega, 1) = 0 \tag{2.1b}$$

$$\int_0^1 M(\omega, y)\, dy = 0 \tag{2.1c}$$

for all ω.

While our primary focus is on the effect of midlatitude eddies, diabatic effects may be of importance in the NAO and annular modes, particularly at lower frequencies. Momentum conservation is ultimately regulated by dissipation at the surface, where on average there can be no net transfer of momentum. Assuming an effective drag coefficient, c_d, independent of latitude, we have

$$\int_0^{\pi/2} c_d \langle \overline{u}_s \rangle d\theta = 0, \tag{2.2}$$

where θ is the latitude and $\langle \overline{u} \rangle_s$ the time and zonally averaged surface wind. In constraint (2.1c), we further assume that there is no significant exchange of net momentum between atmosphere and surface at any time, so that $\langle \overline{u} \rangle_s$ can be replaced by the zonally averaged wind, $\overline{u}_s$.

Last, we must specify a probability space to govern the randomness of M. For simplicity, let us begin with a discrete random walk formulation. Consider a random walk of N steps from $y = 0$ to 1. At each step, the path moves forward $1/N$ units in y and to the left or right d units with equal probability. As we begin at the origin, all 2^N possible paths satisfy (2.1a). Only a fraction of them, however, will be bridgelike in that they both begin and end at the same point. To satisfy (2.1b), the path must take an equal number of steps to the left as to the right. Hence N must be even, and, from combinatorics, we deduce that only $N!/[(N/2)!]^2$ are possible. The final condition, (2.1c), further limits the number of paths. We find that N must be a multiple of 4 for any such mean zero, bridgelike paths to exist. While we do not present a formula for determining the number of them, it is easily computed by exhaustion for small N, and values are listed in Table 1. This subset of paths is a discrete implementation of the process M; each path is a possible jet anomaly profile. By construction, each potential anomaly pattern is equally likely to occur, providing a well-defined probability measure on the subset.

TABLE 1. Number of possible random walks of length N. Note that all walks begin at the origin, and so trivially satisfy (2.1a).

N	Satisfying (2.1a)	Satisfying (2.1a), (2.1b)	Satisfying (2.1a)–(2.1c)
4	16	6	2
8	256	70	8
12	4096	924	58
16	65 536	12 870	526

Formally, one could obtain Brownian motions from these random walks by allowing N to go to infinity and setting the right and left step size $d = \sqrt{1/N}$. By the central limit theorem, the distribution of the position of the path at any y between 0 and 1 will be Gaussian, and this choice of d sets the mean and variance of the distribution to 0 and y, respectively. This particular limit of the random walk is the Wiener process, $W(\omega, y)$, the canonical Brownian motion. The fraction of paths satisfying the first two conditions becomes smaller as N increases, even though the number of such paths is growing. In the limit $N \to \infty$, there will be an infinite number of bridgelike paths, but they will occupy a set of measure zero inside the set of all possible Wiener paths. The same holds for paths satisfying all three conditions. There are an infinite number of mean zero, bridgelike paths, that is, realizations of M, but they occupy a set of measure zero within the set of paths satisfying the first two conditions. Noting these points, we use the Wiener process, which is well developed in the literature, to construct the probability space of M.

We first sketch the procedure by which a realization of M is obtained from a realization of W, as illustrated in Fig. 1. We begin with a Wiener path W (curve a) that trivially satisfies (2.1a). We then detrend W to satisfy the second endpoint constraint, (2.1b). The resulting path, B (curve c) is a realization of a process known in stochastic calculus literature as a "Brownian Bridge,"

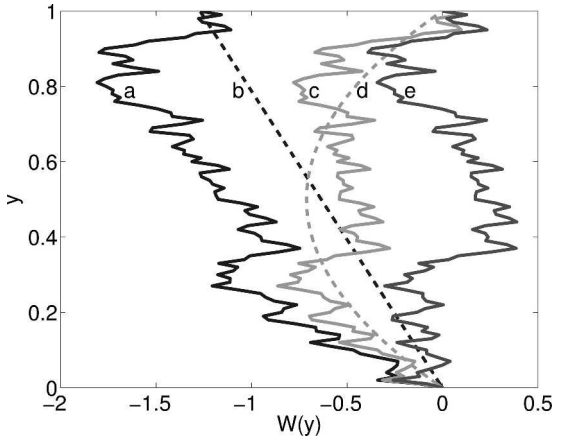

FIG. 1. A sketch of the procedure of transforming a Wiener path to a path of M. Line a is one realization, $W(\omega^*, y)$, of the Wiener process. Line b is the expected, or average, path taken by all Wiener paths that end at $W(\omega^*, 1)$. Line c is the Brownian bridge $B(\omega^*, y)$, formed by taking the difference between lines a and b. Curve d is the expected path taken by all Brownian bridges that have the same integral in y as $B(\omega^*, y)$. Line e is the mean zero Brownian bridge $M(\omega^*, y)$, formed by subtracting lines d from c.

as it arches from (0, 0) to (0, 1). Last, we eliminate the mean in y from B to satisfy (2.1c), thus attaining a realization of M (curve e).

To establish notation, given a function $f(\omega, y)$, we define its expectation,

$$E[f(\omega, y)] = \int_\Omega f(\omega, y) P_W(\omega)\, d\omega, \tag{2.3}$$

where Ω is the space of all ω and $P_W(\omega)$ is the Wiener probability density function. The $E[f(\omega, y)]$ is the expected, or average, value of f at y. The conditional expectation of f, given $Z = z$, $E[f(\omega, y)|Z = z]$, is the expected value of f computed over the subset of Ω where the event $Z = z$ is true.

A construction of B from W is well known in the literature (e.g., Karatzas and Shreve 1991, 358–360). We begin with a realization of the Wiener process, $W(\omega^*, y)$ on the interval 0 to 1. Here ω^* is marked with an asterisk to stress that this is a single path, and so fixed when an expectation with respect to ω is computed. Here $B(\omega^*, y)$ is constructed by detrending $W(\omega^*, y)$ with the *average* path taken by all Wiener paths $W(\omega, y)$ that terminate at $W(\omega^*, 1)$, that is,

$$B(\omega^*, y) \equiv W(\omega^*, y) - E[W(\omega, y)|W(\omega, 1) = W(\omega^*, 1)] \tag{2.4}$$

$$= W(\omega^*, y) - yW(\omega^*, 1). \tag{2.5}$$

It can be shown that (2.5) yields the most general space of Wiener paths, or Brownian motions, that satisfy the fixed end-point constraint, $B(0) = B(1) = 0$.

Equivalently B can be generated from a sinusoidal basis (Knight 1981, 12–14),

$$B(\omega, y) = \frac{\sqrt{2}}{\pi} \sum_{n=1}^{\infty} \frac{\zeta n}{n} \sin(\pi n y), \tag{2.6}$$

where the ζ_n are identically and independently distributed Gaussian variables with zero mean and unit variance. With this formulation, we may more intuitively define the space of ω: an infinite-dimensional vector space of independent Gaussian random variables:

$$\omega = (\zeta_1, \zeta_2, \ldots). \tag{2.7}$$

We will see shortly that it is really only the first few degrees of freedom that govern the small wavenumbers that matter for our question.

We construct M from B by employing a similar procedure as was used to construct B from W. That is, we subtract from a realization of B the expected path taken by all Brownian bridges that have the same integral. Given a specific Brownian bridge, $B(\omega^*, y)$, let $\mu(\omega^*)$ be its mean:

$$\mu(\omega^*) = \int_0^1 B(\omega^*, y)\, dy. \tag{2.8}$$

We then obtain a mean zero Brownian bridge, $M(\omega^*, y)$, using

$$M(\omega^*, y) \equiv B(\omega^*, y) - E\left[B(\omega, y) \left| \int_0^1 B(\omega, y)\, dy = \mu(\omega^*) \right. \right] \tag{2.9}$$

$$= B(\omega^*, y) - 6\mu(\omega^*) y(1 - y). \tag{2.10}$$

The computation from (2.9) to (2.10), that is, computing the expected path taken by all Brownian bridges with mean $\mu(\omega^*)$, is shown in the appendix. The Fourier decomposition of M is

$$M(y) = \frac{\sqrt{2}}{\pi} \sum_{n=1,3,\ldots}^{\infty} \left[\left(\frac{1}{n} - \frac{96}{n^5 \pi^4} \right) \zeta_n - \frac{96}{n^3 \pi^4} \sum_{m=1,3,..m\neq n}^{\infty} \frac{\zeta_m}{m^2} \right] \sin(n\pi y) + \frac{\sqrt{2}}{\pi} \sum_{n=2,4,\ldots}^{\infty} \frac{\zeta_n}{n} \sin(n\pi y). \tag{2.11}$$

It is interesting to observe that all even Fourier modes have been unaffected in the transform, as they are naturally mean zero.

Fundamentally M is different from W and B in that it is not Markovian. That is to say, W and B can be formulated as diffusion processes in which the evolution of the system in space depends only on the current state of the system, but evolution of paths of M depend on the

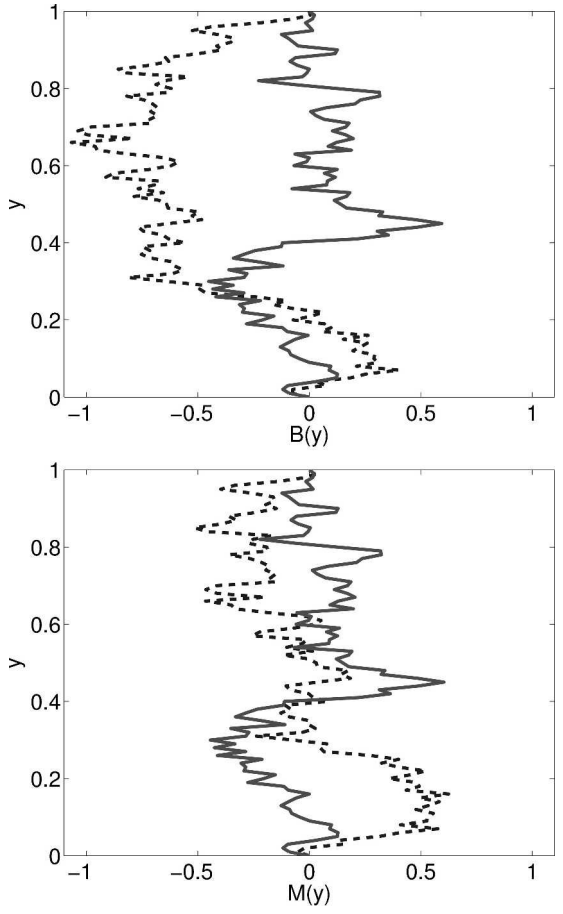

FIG. 2. (top) Two sample paths of $B(\omega, y)$ and (bottom) the corresponding paths of $M(\omega, y)$ constructed as detailed in the text.

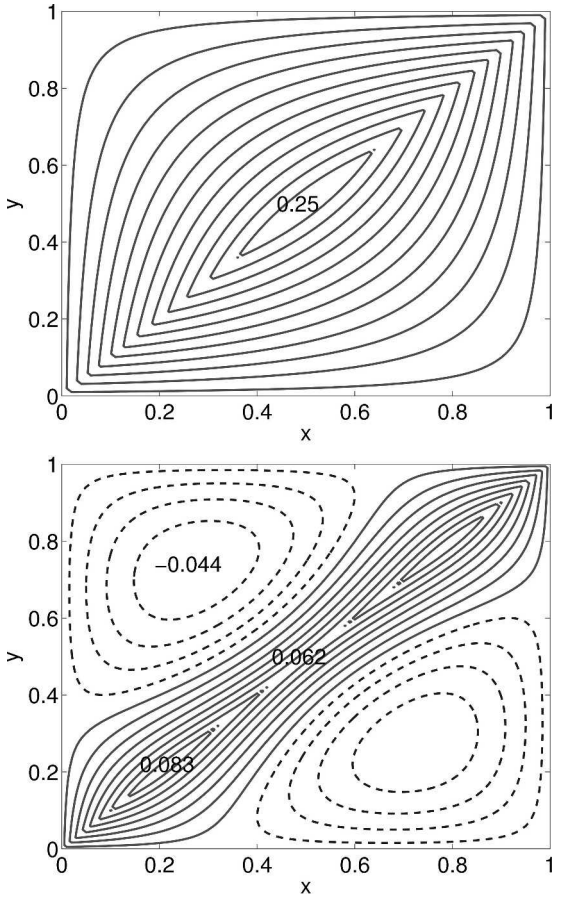

FIG. 3. Covariance function of (top) B and (bottom) M. Positive contours are solid and negative dashed. The contour interval is 0.02 for B, with contours (. . . , −0.01, 0.01, 0.03, . . . ,) and 0.1 for M, with contours (. . . , −0.005, 0.005, 0.015, . . . ,).

entire history of the process. In generating M from B, we have assured that M satisfies (2.1), but we have not proven that M is the most general Brownian motion satisfying them. Numeric results, in which we sample large numbers of Brownian bridges, accepting only those with absolute mean smaller than a threshold ε, suggest that this is, in fact, the most general formulation.

b. Results

In Fig. 2 we show realizations of each process. Both M and B are anomaly patterns, that is,

$$E[B(\omega, y)] = E[M(\omega, y)] = 0 \tag{2.12}$$

for all y so that, on average, paths of both integrate to zero in y. Paths of M, however, integrate to zero in y for every ω (2.1c). The effect of this strict conservation of momentum is clear in their covariance functions, shown in Fig. 3. As M and B are mean zero in ω, the covariance function (e.g., of M) is the expectation

$$\mathrm{cov}(x, y) = E[M(\omega, x)M(\omega, y)]. \tag{2.13}$$

The diagonal $y = x$ of the covariance function shows the variance of the process as a function of y. For the Brownian bridge, the variance is largest at the midpoint, where B is the least constrained. For M, however, variance is slightly suppressed at the midpoint, peaking at $y = 0.25$ and 0.75. Vertical (or horizontal) lines in the covariance function are single-point covariance maps. For example, the line $x = 0.5$ shows the covariance of all points with respect to the process at 0.5. For the Brownian bridge, the covariance function is strictly positive. The only drift of B, on average, is toward 0 at the endpoints; if it is known to be positive (negative) at any point, it is expected to be positive (negative) over the whole domain. For M, however, the covariance function is not always positive. When two points are close, a positive correlation is observed, reflecting the continuity of M in y. As the distance between the points increases, however, the covariance becomes negative. This is a reflection of the fact that, for a profile to be mean zero when it is positive in one region, it must be

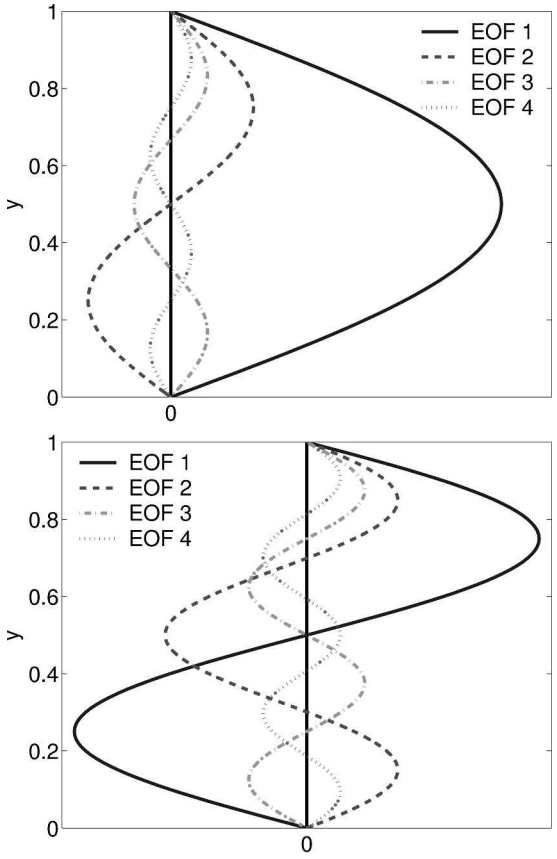

FIG. 4. First four EOFs of (top) $B(\omega, y)$ and (bottom) $M(\omega, y)$. The EOFs (and EOFs in all subsequent figures) are normalized by the variance accounted for by each mode.

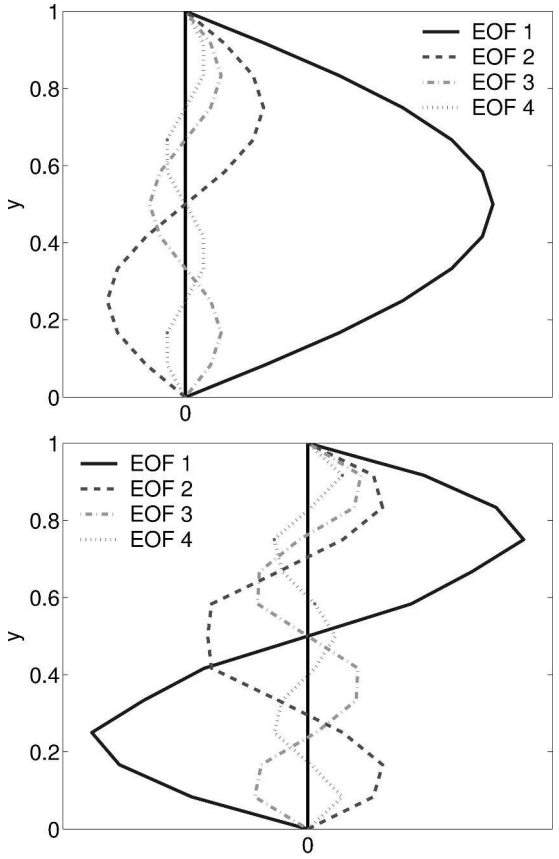

FIG. 5. First four EOFs of a 12-step random walk constrained by (top) (2.1a) and (2.1b) and (bottom) (2.1a)–(2.1c).

negative elsewhere; that is, a westerly anomaly in one region must be balanced by easterly anomaly elsewhere. The single point covariance maps of points near 0.25 and 0.75 indicate a dipole pattern, whereas points in the middle exhibit tripoles.

These differences in the covariance functions manifest themselves in the corresponding EOFs, as demonstrated by Fig. 4. As the Fourier coefficients of B are independent, as shown in (2.6), the sine modes are the natural way to decompose the motion of the Brownian bridge. For M, however, only the even modes are perfect sinusoidal functions. The mean zero constraint mixes the odd Fourier modes together, and they are recombined to be orthogonal in both y and ω space. Most importantly, the first sine mode, which is inherently not mean zero, has been lost; the integral constraint has removed a degree of freedom from the system, eliminating this mode. The remaining odd modes are reorganized so that each is mean zero. The dipole pattern is now the gravest mode allowed by the system and takes position as the foremost EOF.

As a measure of the robustness of these results, we return to the discrete random walk. For the case $N = 12$, there are 924 possible bridgelike paths and 58 mean zero, bridgelike paths. The top EOFs describing the space of these walks are shown in Fig. 5. Even at such course resolution the dipole pattern is clearly the dominant mode of variability in the fully constrained case.

c. Comparison with observations

The National Centers for Environmental Prediction–National Center for Atmospheric Research (NCEP–NCAR) reanalysis data were obtained from the National Oceanic and Atmospheric Administration–Cooperative Institute for Research in Environmental Sciences (NOAA–CIRES) Climate Diagnostics Center, Boulder, Colorado, from their Web site (http://www.cdc.noaa.gov/). The reanalysis procedure is described by Kalnay et al. (1996). We used the 0.995 σ-level zonal winds sampled every 6 h from 1958 to 1997 on a 2.5 $\times$ 2.5 latitude–longitude grid. After the zonal average was taken at each time step, the annual average was computed and smoothed by a 30-day running mean. EOFs were then calculated from the residual winds left after

the removal of the smoothed annual cycle. The covariance matrix was weighted appropriately to account for the decrease in area with latitude (North et al. 1982a).

Surface winds were chosen for comparison as they provide the best indication of the barotropic circulation driven by midlatitude eddies. The top EOFs of the Southern Hemisphere are shown in the top panel in Fig. 6. They are quite consistent with those describing M; EOF analysis has performed a Fourier-like decomposition of the winds, and the first mode is the dipole pattern.

In the bottom panel of Fig. 6 we show the top EOFs of the angular momentum of the Southern Hemisphere barotropic flow,

$$\Phi(\theta) = r_0 \overline{u}_s(\theta) \cos^2\theta, \tag{2.14}$$

where θ is latitude, r_0 is the radius of the earth, and $\overline{u}_s$ is the zonally averaged surface wind. One would expect the angular momentum to provide the best comparison with model predictions. With the exception of the second EOF, this is largely the case. The $\cos^2\theta$ factor focuses the activity in lower latitudes where the subtropical jet may play a larger role. This may explain in part the skewness of the second EOF, where the equatormost lobe of the tripole is disproportionately large.

The observational results are extremely robust. For both the zonal winds and implied angular momentum, the results remain largely the same when 1) analysis is restricted to half of the time record, 2) linear trends are removed, 3) the degree of smoothing of the seasonal cycle is increased or decreased, and 4) the dataset is restricted to a particular season (i.e., winters only). Similar results are also obtained from analysis of the Northern Hemisphere surface winds and the zonally and vertically averaged zonal winds of both hemispheres. With the vertically integrated winds there appears to be a greater degree of mixing between the dipole and tripole EOFs, so that in a few cases the top two EOFs are both skewed tripole patterns. The dipole structure of the first EOF is further corroborated by other authors in more extensive studies of the observed winds (Lorenz and Hartmann 2001; Feldstein and Lee 1998).

The fractions of the total variance represented by the top EOFs of the various models and reanalysis data are shown in Table 2. With B and M, the variance represented by EOFs of wavenumber n decay as n^{-2}, as can be seen from Eqs. (2.6) and (2.11). The variance accounted for by the top EOFs is relatively independent of resolution, but the total variance, and hence the relative variance described by each mode, is altered when small scales are truncated. Hence the top EOFs of the constrained 12-step random walks explain a larger fraction of the variance. The variance represented by EOFs of V04 and the reanalysis data appear to decay exponentially with wavenumber n, suggesting that the dynamics are producing a smooth profile, in which both the function and its derivatives are continuous.

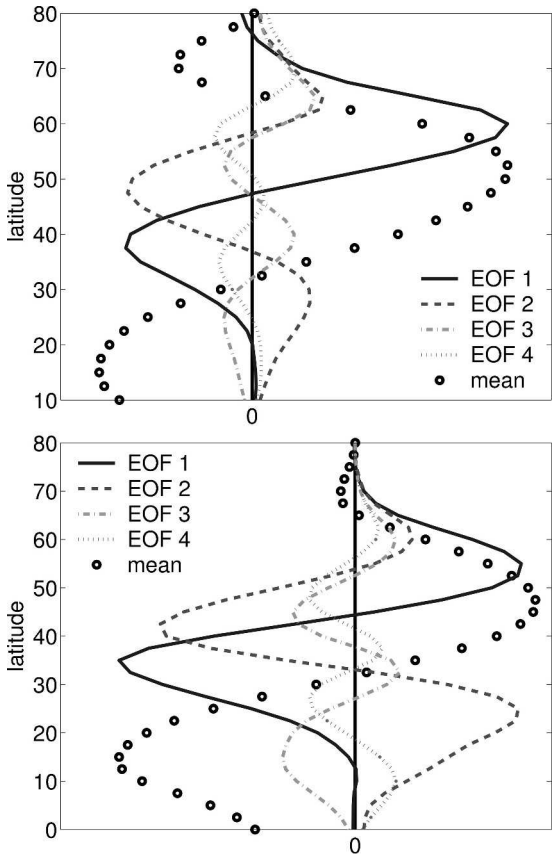

FIG. 6. First four EOFs of (top) the NCEP–NCAR reanalysis surface winds and (bottom) angular momentum. The "mean" curves refer to the climatological surface winds and angular momentum, respectively, scaled for ease of comparison with the EOFs.

As a consequence of choosing Brownian motion to model the anomalous zonal wind, we have assumed that the underlying vorticity anomalies are white in space. The zonally averaged vorticity anomalies implied by M show no preference for any scale. Formally, this can be seen from (2.11), where every Fourier mode of $-dM/dy$ (with the exception of the first) will have nearly equal weighting. Given that we also neglect spherical effects, the match between M and the reanalysis winds in the Southern Hemisphere is perhaps a bit fortuitous. One might expect the EOFs of the angular momentum to better compare with the predictions of the model, as it is the conserved quantity. Here the second EOF appears to be stronger at the expense of the first. While EOFs of the Northern Hemisphere winter winds have the same structure as those in the Southern Hemisphere, the relative importance of the modes differs. For the zonal wind, there is more energy in

TABLE 2. Percent variance represented by the top EOFs. RW-B refers to the 12-step random walk constrained to be bridgelike and RW-M the same walk further constrained to be mean zero. V04 refers to the EOFs of the zonally averaged zonal wind of their zonally symmetric barotropic model. The Southern Hemisphere values for the EOFs of u_s and Φ are based on the full dataset. In the calculations of the Northern Hemisphere winds, only data from the winter months [Dec–Jan–Feb (DJF)] were used.

No. of nodes	$B(\omega, y)$	$M(\omega, y)$	RW-B	RW-M	V04	SH u_s	SH Φ	NH u_s	NH Φ
0	60.7	—	61.6	—	—	—	—	—	—
1	15.2	38.0	15.6	42.2	51.1	37.0	31.1	32.0	43.4
2	6.8	18.6	7.2	18.7	26.6	21.3	27.6	21.7	23.3
3	3.8	9.5	4.2	11.5	10.9	9.8	11.3	12.2	7.9

higher EOFs, while the EOFs of angular momentum more closely match the values predicted by M.

3. A two-dimensional model

a. Theory

We now turn to the zonal structure of EOFs and correlation functions by constructing a simple two-dimensional model using the process M as a source of variability. In particular, we seek to understand the robust appearance of apparent annular modes in EOF analyses, despite the general absence of annular patterns in single-point correlation maps and other measures of zonal correlation.

In V04, it was shown that anomalous stirring of the vorticity (i.e., anomalous baroclinic eddies in the atmosphere) leads to anomalous convergence of momentum, and hence a dipole anomaly in the streamfunction. While this theory only applies strictly to the zonally averaged flow, as long as the zonal averaging is sufficient to cover a few eddies, the result approximately holds. Thus enhanced stirring in one region, for example, a storm track, leads to enhanced variability in that region and an NAO-like pattern. We approximate this process by directly simulating the local zonal flow (by which we mean flow in the neighborhood of one longitude) with the process M. We then specify the correlation of the field in the zonal direction, seeking to replicate the local structure observed in the single-point correlation maps of models and observations.

While M was constructed to simulate anomalies of the zonally averaged barotropic wind, we can also use the process to simulate the local reorganization of zonal momentum by eddies. Any longitudinal zonal wind profile in a two-dimensional, incompressible random flow field applicable to the extratropical atmosphere should obey constraints (2.1). The end-point constraints still apply if we continue with the assumption that the variation of the flow in the Tropics is weak. Assuming there is no flow across the equator, continuity implies that the latitude-integrated flow is independent of longitude, establishing (2.1c).

b. The model

We begin with a simple discrete example and then generalize to a larger class of momentum-conserving flows. For simplicity we simulate the flow in a channel with zonally periodic boundaries. Suppose there are n_f degrees of freedom in the channel; that is, given a channel of length L and length scale of eddy anomalies L_e, n_f is of order L/L_e. To generate one realization of the flow field, n_f-independent realizations of M, denoted m_j, $j = 1, 2, \ldots, n_f$, are sampled. The flow at n_f-representative longitudes, $\hat{m}_j$, $j = 1, 2, \ldots, n_f$, are then constructed from the m_j. We build in a simple zonal correlation structure, where

$$\begin{aligned} \hat{m}_j &= (1/\sqrt{2})(m_j + m_{j+1}) \quad j \neq n_f \\ \hat{m}_{n_f} &= (1/\sqrt{2})(m_{n_f} + m_1). \end{aligned} \tag{3.1}$$

This structure specifies that the flow at any given longitude is 0.5 correlated with the flow at neighboring longitudes and uncorrelated with all others. For comparison we also construct a null case in which the flow at each of the n_f representative longitudes is uncorrelated with the others: $\hat{m}_j = m_j$.

We first compute numeric solutions. n_f is varied from 2 (where the structure is just that of our one-dimensional process) to 13. In Fig. 7 we compare two snapshots of random fields with $n_f = 8$, one the null case with no zonal correlation and the other described by (3.1). The zonal correlation of the latter is much easier to detect in single-point correlation maps, Fig. 8. By construction, zonal correlation stretches out one step in either direction from the base point, but no farther. Similar to the single point correlation maps of streamfunction observed in V04, Figs. 9 and 14, a dipole pattern appears when the base point is chosen poleward or equatorward of the jet center but, when points are chosen near the center of the jet, a meridional tripole pattern is observed.

Figure 9 illustrates the percent variance represented by the top 20 EOFs for the null case and the correlated case with $n_f = 8$. With the uncorrelated run, we have tiers of eight degenerate EOFs, corresponding to eight

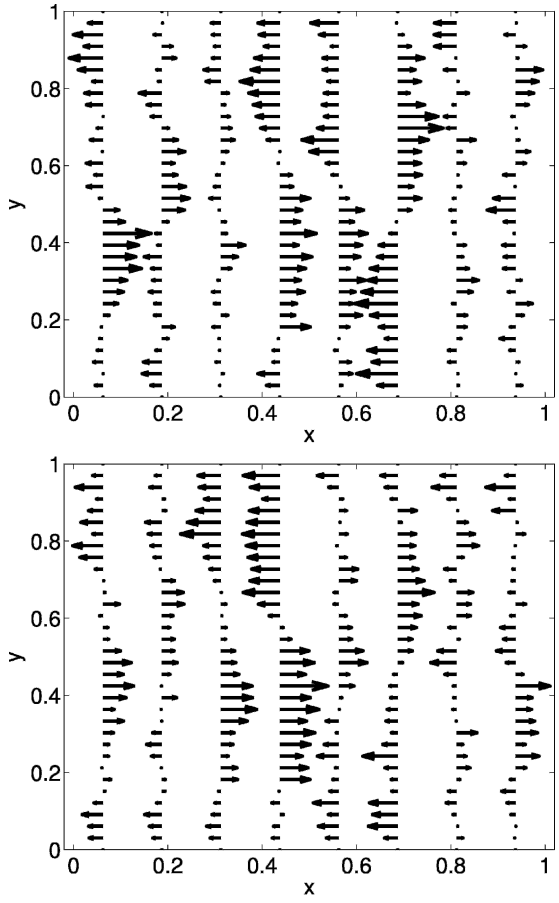

FIG. 7. Realizations of the two-dimensional random flow fields with $n_f = 8$. (top) The null case, with no zonal correlations. (bottom) The flow has the simple correlation described in (3.1). EOFs are computed at discrete grid points indicated by the position of the arrows.

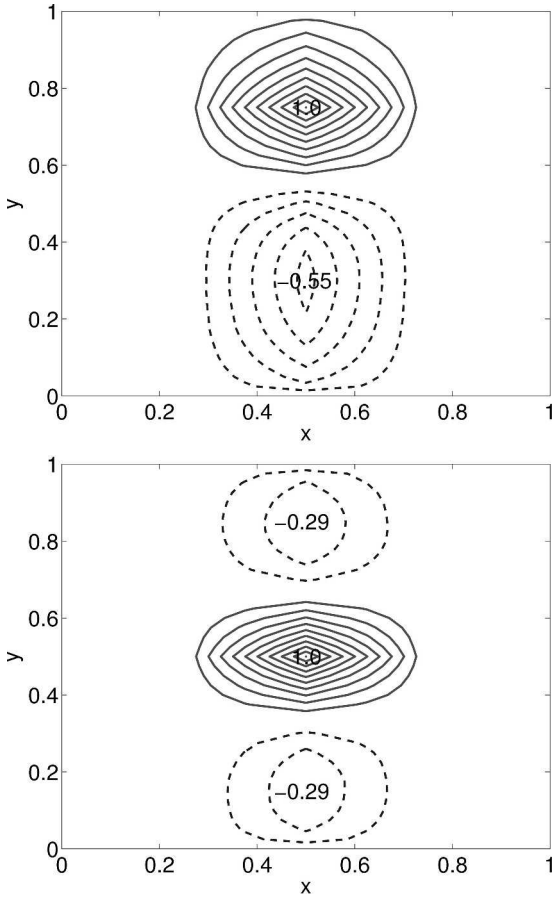

FIG. 8. Single-point correlation maps from the random field with zonal correlation given by (3.1) with $n_f = 8$. The base points are those with correlation (1.0). Contour interval is 0.1, and the zero contour has been omitted. A dipole or tripole pattern is found by varying the position of the base point, as observed in V04 (their Figs. 9 and 14).

independent meridional dipole patterns, tripole patterns, and so forth (none shown). Differences in the variance accounted for by each EOF within the tier reflect the finite length of the simulation and provide a measure of the convergence. The addition of zonal correlation in the second simulation separates one EOF above the rest: an annular mode–like structure shown in Fig. 10. Deviation from perfect zonal uniformity is a product of the finite sampling. The next two EOFs (not shown) are also meridional dipole patterns but with zonal wavenumber 1. The two are degenerate and in quadrature with each other; their phase is arbitrary, given the lack of any zonal asymmetry in the model.

The value of n_f does not govern the existence of the annular mode–like EOF in this model, but rather its separation from other modes. The annular mode–like pattern is always the first EOF, but its separation from higher wavenumber patterns is a function of n_f, as indicated in Fig. 11. Beyond $n_f = 13$, the wavenumber 0 and 1 patterns are poorly separated and begin to mix in simulations. This could be remedied of course by still larger sampling, but from a practical point of view, such small separation is meaningless. Note that, as n_f increases, the physical system described by (3.1) changes in that the zonal scale of the correlation decreases if one assumes that the zonal scale of the channel is fixed. If one were to appropriately increase the correlation between modes [(e.g., $\hat{m}_j = f(m_{j-1}, m_j, m_{j+1})$] so that the zonal scale of the correlation remained constant relative to the length of the channel, then the first EOF would be expected to remain annular and distinct.

c. Analytic solutions

As the zonal correlation is independent of latitude, the zonal structure of an EOF is independent of the meridional structure. Hence, a two-dimensional EOF can be separated into meridional and zonal components, that is,

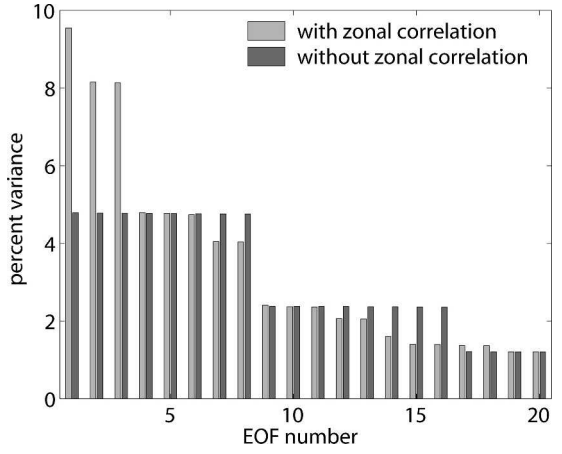

FIG. 9. Percent variance accounted for by top EOFs, $n_f = 8$. Values for the uncorrelated and correlated simulations are shown for comparison. The annular mode–like EOF shown in Fig. 10 is the top EOF of the correlated simulation.

$$\mathbf{E}_{k,l} = \mathbf{V}_l \mathbf{U}_k, \tag{3.2}$$

where matrix $\mathbf{E}_{k,l}$ is the two-dimensional EOF, meridional EOF $\mathbf{V}_l$ is a column vector, and zonal EOF $\mathbf{U}_k$ is a row vector. The subscript k refers to the kth zonal eigenvector, and l for the lth meridional eigenvector. The two-dimensional eigenvalues, $\lambda_{k,l}$, are the product of the meridional and zonal eigenvalues, $\lambda_{k,l} = \lambda_k \lambda_l$. Hence, the fraction of the total variance accounted for by a two-dimensional EOF is given by the product of the fractional variances represented by the zonal and meridional EOFs.

The meridional EOF structure, that of M, was diagnosed in section 2. The zonal EOF structure is determined from the zonal covariance matrix $\mathbf{C}$, where the ijth entry is defined by

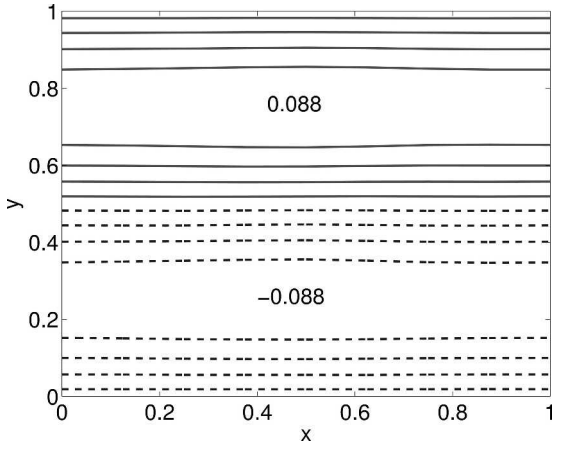

FIG. 10. First EOF of the model with zonal correlation (3.1) and $n_f = 8$, an "annular mode." Contour interval is 0.02, contours (. . . , −0.01, 0.01, 0.03, . . . ,). As shown in analytic computations in section 3c, with infinite sampling the EOF is perfectly uniform in x and sinusoidal in y.

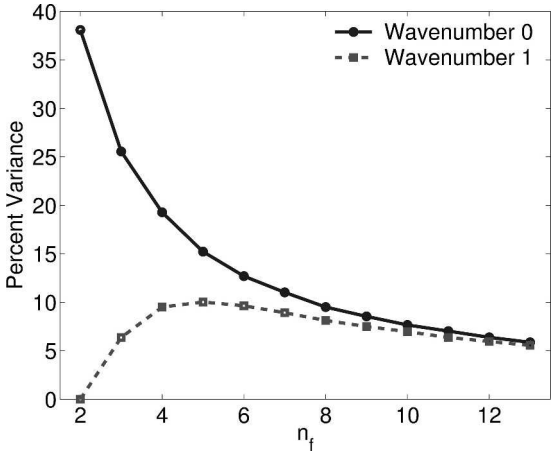

FIG. 11. Percent variance represented by the first (wavenumber 0, solid line) and second (wavenumber 1, dashed line) EOFs as a function of n_f for the model with zonal correlation (3.1).

$$(c_{i,j}) = \mathrm{cov}(\hat{m}_i, \hat{m}_j). \tag{3.3}$$

The zonal correlation matrix $\mathbf{C}$ for the uncorrelated null case is simply the identity matrix. All eigenvalues are degenerate and equal to 1. The sum of all eigenvalues, the trace of the matrix, is n_f, so that each EOF explain $1/n_f$ of the variance. The two-dimensional EOFs then clump in groups of n_f: the first n_f each represent $0.38 \cdot 1/n_f$ of the total variance, the second set $0.19 \cdot 1/n_f$, and so forth. For $n_f = 8$ the corresponding values are 0.048 and 0.023, as observed in the numeric simulation.

For the correlated cases the covariance matrix has three nonzero diagonals (plus nonzero corners, a result of the periodic boundaries),

$$c_{i,j} = \begin{cases} 1 & \text{if } i = j, \\ 1/2 & \text{if } i = j \pm 1 \text{ or } (i,j) = (1, n_f), (n_f, 1), \\ 0 & \text{otherwise.} \end{cases} \tag{3.4}$$

As the sum of each row of $\mathbf{C}$ is 2, a vector of all ones is an eigenvector with eigenvalue of 2. All other eigenvalues are less than 2, so this mode is nondegenerate and the foremost EOF: the annular mode. It explains $2/n_f$ of the zonal variance so that the full two-dimensional annular mode EOF explains $0.38 \times 2/n_f$ of the variance. The n_f^{-1} power law observed in Fig. 11 is thus an expression of the fact that each "annular mode" in this model represents the same amount of variance, but the total variance in the system increases linearly with n_f. The remaining eigenvalues are distributed between 0 and 2, and the wavenumber of the associated eigenvector increases for the smaller values. For $n_f = 8$, the first three eigenvalues are 2, 1.7, and 1.7. The annular mode then accounts for $0.38 \times 2/8 = 0.095$ of the vari-

ance, and the degenerate second and third EOFs, with wavenumber 1, account for $0.38 \times 1.7/8 = 0.081$ of the variance, each.

We can easily compute the EOFs of more general patterns as long as we keep the zonal correlation independent of latitude, so that the meridional and zonal structure of the EOFs remain independent. Rather than mechanically construct the correlations, $\hat{m}_j = f(m_1, \ldots, m_{n_f})$, as in the model above, one may specify the covariance matrix $\mathbf{C}$ directly, or, in the continuous limit, specify the covariance function. EOF analysis is possible provided $\mathbf{C}$ is symmetric and positive semidefinite, and the EOFs themselves (or any rotation thereof) can be used to construct a flow with this zonal structure from the m_j. One can then construct a model with an arbitrarily large number of zonal degrees of freedom, n_f, while maintaining reasonable zonal correlations by filling out the diagonals of $\mathbf{C}$. In the continuous limit, the system can be viewed as a stochastic process on a circle. As discussed by North et al. (1982a), rotational invariance then leads EOF analysis to the trigonometric functions. The ranking of modes follows the same principal as expressed before. A simple red spectrum favors the gravest mode with zero wavenumber: the annular mode.

It is zonal symmetry of the covariance statistics, not necessarily of the motions themselves, that is required to produce an annular pattern. Zonal symmetry of the statistics implies that each row in the matrix is a translation of the others. Any such matrix will exhibit a zonally uniform EOF. A sufficient condition for this to be the dominant EOF is that the covariance decay monotonically over some finite length as the distance between points increases. As illustrated by our discrete model, local correlation—only three nonzero diagonals in the covariance matrix—is sufficient to produce such a pattern. Zonal symmetry of the motions, that is, long distance correlation in the zonal direction, would be manifested by nonzero values filling out the diagonals of the covariance matrix. This too would lead to zonally uniform EOFs, but is not a necessary condition.

4. An NAO-like pattern

In V04, it was observed that enhanced stirring of the vorticity in a particular region led to enhanced local zonal wind anomalies and consequently a NAO-like pattern. We may use our stochastic process to model this, that is, use M to directly simulate the response of the zonal flow to inhomogeneous eddy forcing. For a simple illustration we employ the same $\hat{m}_j = f(m_j)$ structure as in (3.1), but the strength of the random fluctuations of the zonal flow in one region (one m_j) is increased. For $n_f = 8$, we make the following changes:

$$\begin{aligned} \hat{m}_4 &= \sqrt{1/2}\, m_3 + \sqrt{a - 1/2}\, m_4 \\ \hat{m}_5 &= \sqrt{a - 1/2}\, m_4 + \sqrt{1/2}\, m_5. \end{aligned} \tag{4.1}$$

for $a > 1/2$. The corresponding zonal covariance matrix is

$$\mathbf{C} = \begin{bmatrix} 1 & 0.5 & 0 & 0 & 0 & 0 & 0 & 0.5 \\ 0.5 & 1 & 0.5 & 0 & 0 & 0 & 0 & 0 \\ 0 & 0.5 & 1 & 0.5 & 0 & 0 & 0 & 0 \\ 0 & 0 & 0.5 & a & a - 0.5 & 0 & 0 & 0 \\ 0 & 0 & 0 & a - 0.5 & a & 0.5 & 0 & 0 \\ 0 & 0 & 0 & 0 & 0.5 & 1 & 0.5 & 0 \\ 0 & 0 & 0 & 0 & 0 & 0.5 & 1 & 0.5 \\ 0.5 & 0 & 0 & 0 & 0 & 0 & 0.5 & 1 \end{bmatrix} \tag{4.2}$$

so that a sets the variance of the "storm track" region. If we take a to be 2, thus doubling the variability in the storm track, the first three eigenvalues are 3.6, 1.9, and 1.7. The trace of $\mathbf{C}$ is 10 so that the top EOF represents $0.38 \times 3.6/10 = 0.14$ of the total variance. Combining this with the first meridional EOF, we obtain the NAO-like mode shown in Fig. 12. It is well separated from the next EOF, which explains only $0.38 \times 1.9/10 = 0.072$ of the total variance.

Zonal inhomogeneity shifts EOF analysis from an annular pattern to a more localized NAO-like pattern. Figure 13 illustrates the degree to which the EOF has localized as a function of a. As a measure of the asymmetry of the first EOF, we plot the ratio m/M, where m is the minimum of the zonal EOF and M the maximum. For example, in the case when $a = 2$ above, $m/M = 0.0067/0.69 = 0.0096$. For $a = 1$ the variance is equal at all longitudes, and so is the first EOF. When a is 1.25, the variance of the flow is only 25% stronger in one region, but the first EOF weights this region roughly five times as much as on the opposite side of the channel.

In general, the first EOF computed by numerical

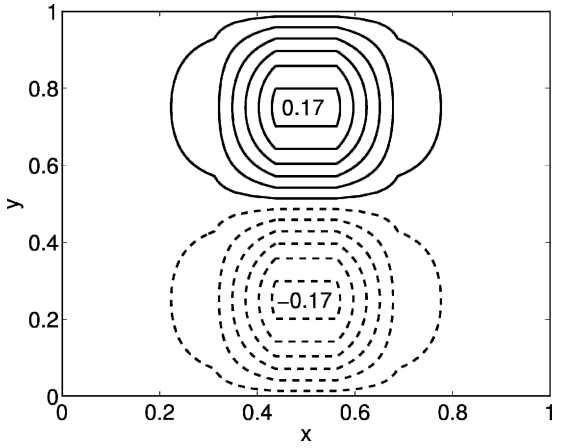

FIG. 12. The first EOF from a simulation with enhanced variability in one region, described by (4.1). Contour interval is 0.03, with contours (. . . , −0.015, 0.015, 0.045, . . . ,). It is NAO-like in being a zonally localized dipole pattern.

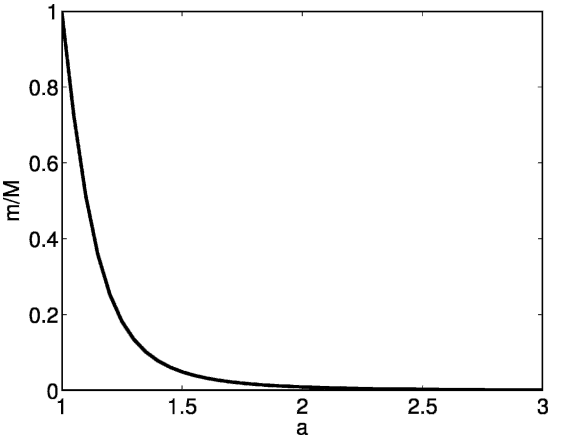

FIG. 13. EOF localization as a function of *a*. *m*/*M* is the ratio of the minimum value of the first zonal EOF to its maximum value, and hence a rough measure of the asymmetry of the mode.

simulation of the two-dimensional model with zonally uniform zonal correlations ($a = 1$) was slow to converge to the analytic solution. The analytic first EOF is zonally uniform, projecting only on to zonal wavenumber 0. The first EOF based on simulation was always dominated by zonal wavenumber 0, but mixed with small wavenumber 1 or higher anomalies. Only with a long simulation did these higher wavenumber patterns disappear. Such slow convergence to a perfect zonal wavenumber-0 pattern was also observed in V04 when the barotropic model was forced with statistically zonally uniform forcing.

The steep slope of the ratio m/M near $a = 1$ in Fig. 13 suggests an explanation for the slow convergence. Zonal EOF patterns are quite sensitive to small inhomogeneities in the covariance matrix. For example, when a is 1.01, so that the variance in one region is just 1% greater than the rest of the domain, the ratio of m/M is 0.94, indicating a 6% zonal inhomogeneity in the top EOF. Coupled with the slow convergence of the experimentally determined covariance matrix,[2] this sensitivity necessitates long simulations to achieve the pure analytical zonal wavenumber-0 structure.

5. Pressure models

How does our decision to model the zonal winds, as opposed to another variable, affect our conclusions? To answer this question, we formulate two simple models of the zonally averaged surface pressure to compare with our model M of the zonally averaged zonal winds. By hydrostatic balance, surface pressure provides a measure of the vertically integrated mass of the atmosphere. Conservation of mass then establishes a constraint on the zonally averaged surface pressure. What does this constraint imply in the selection of an EOF basis?

a. Model P_1

Using the same notation as for $M(\omega, y)$ in section 2a, we construct the stochastic process $P_1(\omega, y)$ to model the space of zonally averaged surface pressure anomalies. To enforce the conservation of mass, we require that all anomalies have zero mean, thus constructing a model of the zonally averaged pressure in a homogeneous channel. We further assume there is no surface pressure anomaly at the equator (the lower boundary of the channel), in keeping with our thinking that the NAO and annular modes are primarily midlatitude phenomena. The process is then very similar to M, but for the omission of constraint (2.1b), which pins the zonal winds to zero at the pole. Paths are constructed from the Wiener process by the same procedure used to obtain M from B:

$$P_1(\omega^*, y) = W(\omega^*, y) - E\left[W(\omega, y) \left| \int_0^1 W(\omega, y)\, dy \right. \right. = \left. \left. \int_0^1 W(\omega^*, y)\, dy \right] \right. \tag{5.1}$$

$$= W(\omega^*, y) - \left[\int_0^1 W(\omega^*, y)\, dy \right] \frac{3y}{2}(2 - y). \tag{5.2}$$

[2] The magnitude of the absolute error between the estimated covariance matrix (i.e., the covariance matrix computed from a finite simulation with n independent observations) and the true covariance matrix decays with the square root of the number of independent observations, $n^{-1/2}$.

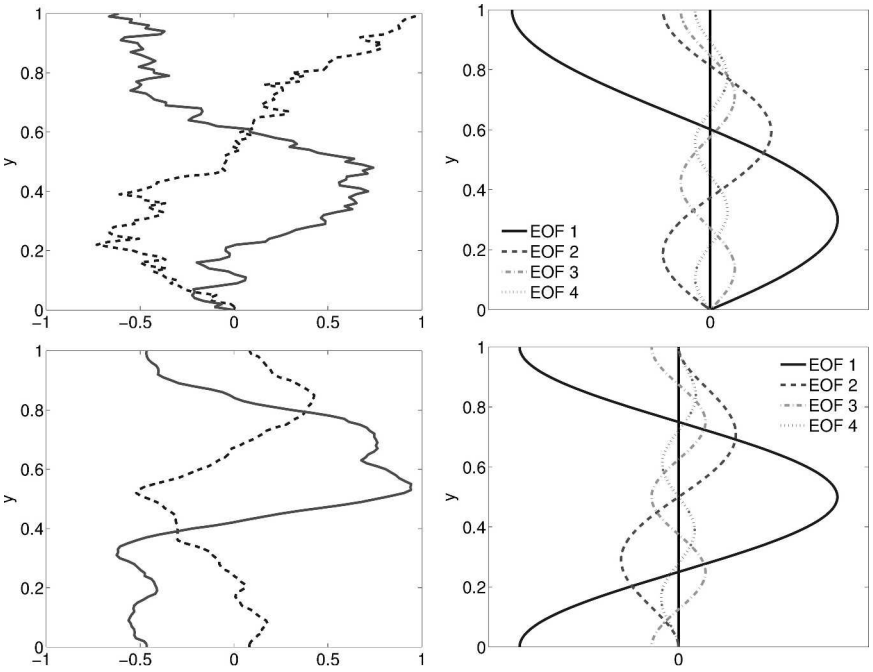

FIG. 14. (left) Sample paths from models (top) P_1 and (bottom) P_2. (right) The first four EOFs of the two respective models.

Computation of the expected path taken by all Wiener paths of a given mean and the Fourier decomposition of P_1 are discussed in the appendix. Realizations of P_1, which are just Brownian motions constrained to have zero mean, are shown in Fig. 14.

Also shown in Fig. 14 are the top EOFs of model P_1. The first EOF is a dipole of pressure: an annular mode. We again have a Fourier-like decomposition of the field, but now EOFs take the form of $\sin[\pi(n + 1/2)]$, modified so that each has zero mean. Individual paths of P_1 are not differentiable, so one cannot speak of the geostrophic wind implied by individual realizations. The EOFs are differentiable; the geostrophic winds implied by the first indicate a dipole in the wind, the second a tripole, and so forth. The implied winds, however, neither conserve momentum nor decay to zero at the equator and the pole.

The use of Brownian motion as our starting point makes it problematic to improve this model to account for the constraints on the zonal wind. We cannot enforce the conservation of momentum without the existence of geostrophic winds on a path by path basis, and it is the coupling of momentum conservation with continuity that allows us to extend our model of M to two dimensions in section 3. There are of course a number of differentiable stochastic processes that would enable us to overcome this limitation. To avoid the introduction of new mathematics, however, we explore one option based on our previous work with M.

b. Model P_2

Realizations of our second model of the zonally averaged surface pressure, $P_2(\omega, y)$, are obtained from paths of M by integration, so inheriting geostrophic winds satisfying constraints (2.1):

$$P_2(\omega^*, y) = c(\omega^*) + \int_0^y f_0 M(\omega^*, x)\, dx, \qquad (5.3)$$

where f_0 is the Coriolis parameter (assumed to be constant) and $c(\omega)$ is an integration constant determined on a path by path basis to ensure that each realization has zero mean. While $c(\omega)$ enforces the conservation of mass, it also eliminates our control of the pressure at the equator; pressure profiles are now free at both ends. The loosening of boundary conditions can be seen in the sample paths of P_2 and the corresponding EOFs shown in the bottom panels in Fig. 14. The Fourier decomposition of P_2 is shown in the appendix.

Given the one-to-one relationship between paths of P_2 and M, it is not a surprise that there is a one-to-one correspondence between their EOFs. The EOFs of M are exactly the geostrophic winds implied by the EOFs of P_2. What is perhaps of interest are the variances represented by each EOF, shown in Table 3. EOF 1 corresponds to the same motion in P_2 and M, but the first EOF of pressure explains a much larger fraction of the variance, 65% as compared to 38%.

Pressure, as the *integral* of the zonal winds, contains

TABLE 3. Percent of the variance represented by the top pressure EOFs. EOFs of the Southern Hemisphere are computed from reanalysis sea level pressure (SLP) observations between 0° and 80°S. EOFs of the Northern Hemisphere are based on wintertime (DJF) observations from 0° to 90°N.

EOF	$P_1(\omega, y)$	$P_2(\omega, y)$	SH SLP	NH SLP
1	50.2	64.7	60.9	51.3
2	17.0	26.5	19.0	25.2
3	8.5	4.0	8.3	11.5

more energy in larger scales. In these idealized models, this can be seen in the decay rates. While the variance of EOFs of M decay with wavenumber as n^{-2}, they decay as n^{-4} for P_2. The increased dominance of the first EOF of model P_1 relative to M, however, does not follow from the same reasoning; both are Brownian motions with n^{-2} decay. Rather, it is a function of the wavenumbers allowed by the systems. Motions with wavenumbers 1, 3/2, 2, . . . are allowed in M, while P_2 is characterized by 3/4, 5/4, 7/4, ... Albeit the n^{-2} decay is strictly true only in the limit as $n \to \infty$, it applies roughly to the small wavenumbers. Hence, the ratio of the variances of the first two EOFs can be estimated by $(5/3)^2 \approx 2.8$ for P_1 as compared to $(3/2)^2 = 2.25$ for M.

c. Comparison to observations

NCEP–NCAR reanalysis sea level pressure data were obtained in the same form as the surface zonal winds and EOFs computed with the same procedure. In Fig. 15 we show the EOFs of sea level pressure in the Southern Hemisphere. Data over Antarctica (poleward of 80°S) were omitted in these calculations, but repeat computations with the full hemispheric pressure field produced nearly identical results. As seen with the zonal winds, the EOF patterns are very robust. The same EOFs are observed in computations based on subsets of the time record, and in similar analysis of the Northern Hemisphere. The percent variance represented by the top EOFs are listed in Table 3. The first EOF in the Northern Hemisphere winter is less dominant than its southern counterpart. This difference appears to be relatively independent of the data used to compute the EOF; similar results are found when observations are limited to a season in the Southern Hemisphere or extended to the whole year in the Northern Hemisphere.

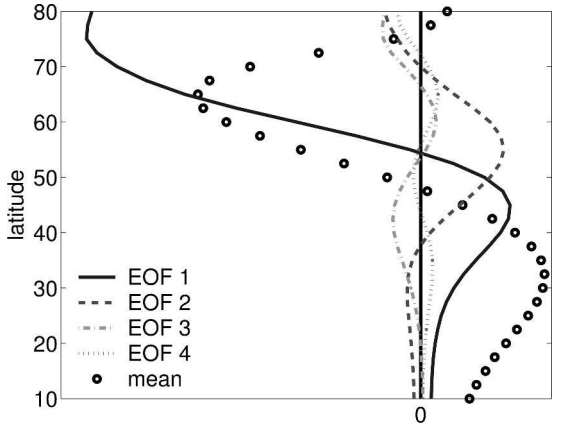

FIG. 15. Top EOFs of sea level pressure in the Southern Hemisphere. Data poleward of 80°S were omitted from the calculation. The mean sea level pressure is shown as the anomaly from the hemispheric mean and scaled for comparison with the EOFs.

Model P_1 performs much better in capturing the basic structure of the observed EOFs. EOF analysis is quite sensitive to boundary conditions; the modes describing P_2 must satisfy constraints on their derivatives, and the cosinelike modes capture the end point constraints on the geostrophic winds. This is not to say that conservation of momentum and mass are competing effects. Rather, both constraints aid in the selection of the dipole EOF. A more complex model could integrate both constraints, as done naturally by atmospheric motions.

As seen in Table 3, the relative importance of the top EOFs in the atmosphere fall between models P_1 and P_2. It is somewhat problematic that both models M and P_1 so closely match the variance structure of atmospheric EOFs. Given geostrophic balance, it is not possible for both the winds and pressure to be described by Brownian motion. Spherical geometry is more important for the surface pressure than zonal winds (North et al. 1982b) so that comparison of models P_1 and P_2 to the atmosphere is more tenuous; the result may be the product of canceling errors. Also, the reanalysis winds and pressure EOFs appear to decay exponentially with wavenumber. The differences in the relative importance of EOFs between model M and P_2 is a result of low order algebraic decay. With exponential decay, the top EOFs of both pressure and winds can explain the same fraction of the variance. The atmosphere is likely somewhere in between these extremes.

What do these pressure models say about our initial question concerning the impact of variable choice on EOF analysis? Perhaps the most important point is seen in Tables 2 and 3, where we find the top EOFs of pressure, the annular modes, to be more dominant than the top EOFs of zonal wind. In the atmosphere fields are noisier and the decorrelation spectrum is not monotonic. The robustness of EOFs hinges on their separation. The larger separation between the top pressure EOFs makes it more probable for the zonally averaged signal to remain distinct in a noisy two-dimensional field. There is less separation between scales in the

zonal winds, and consequently the annular signal is more likely to be overwhelmed.

6. Discussion and conclusions

We have constructed a series of stochastic models to determine the implications of the symmetries of the eddy-driven, barotropic circulation in the selection of an EOF basis. Previous studies by Obukhov (1947), Batchelor (1953), and North and Cahalan (1981) have illustrated the effects of topological symmetries and decorrelation structure on an EOF basis constructed to describe random motions. We have added information about the fluid dynamics—in particular that mass and momentum be conserved—to models of random motions. We show that in various cases the resulting EOFs and correlation structures resemble those of the atmosphere. Meridional dipole structures robustly arise in both EOF and correlation analysis and, depending on the zonal correlation structure of the stochastic model, either zonally elongated or zonally localized EOFs resembling annular modes and the North Atlantic Oscillation, respectively, are found. Zonally uniform EOFs arise when the zonal correlation is independent of longitude and decays monotonically with zonal distance, but do not require hemispheric-scale correlations for their existence.

In our simplest model, M, we explored the space of zonally averaged barotropic wind anomalies by constructing Brownian motions that are consistent with observed anomalies in a channel, specifically the conservation of zonal momentum. This constraint proved pivotal in the determination of the EOF basis. The result is a dominant meridional dipole pattern similar to that observed in the NAO and AO. The dipolar sinusoidal pattern is the gravest mode that satisfies the integral constraint required by the conservation of momentum. With this stochastic process, the dipole pattern is not indicative of a dynamical oscillation. Rather, it is part of a Fourier-like decomposition, the most efficient statistical expression of the variability. The EOF patterns predicted by the model are similar to those observed, as shown in section 2c.

The two-dimensional model illustrates a second important point. While zonally symmetric motions are sufficient to produce annular patterns of variability, they are not necessary. The necessary condition for zonally uniform EOFs is zonal symmetry of the covariance statistics. Our model makes explicit a case where the motions are not symmetric, as seen in the finite zonal correlation patterns, Fig. 8, but zonal symmetry of the statistics produces the annular mode, Fig. 10. Ambaum et al. (2001) make a similar point with a low-order model of the Arctic Oscillation.

We also found that the EOF structure of the two-dimensional model was quite sensitive to small asymmetries in the covariance statistics. In particular, if we increase the variance in the stochastic model in a zonally localized region, the annular EOFs are replaced by EOFs that resemble those of the NAO, as shown in Fig. 12.

Last, we compared models of surface pressure to models of the zonal wind. Our first model, P_1, is similar in spirit to M, consisting of Brownian motions constrained to behave as anomalies of the zonally averaged surface pressure. In particular, anomalies must conserve mass. EOF analysis again produces Fourier-like modes consistent with the essential constraints and boundary conditions; the first and gravest mode is a dipole in pressure, or mass, between the pole and lower latitudes. Both the EOF patterns and the variance represented by each mode compare well with reanalysis observations.

Our second pressure model, P_2, was based directly on M in an effort to account for constraints on both the zonal winds and pressure. While the model does not predict the observed EOF structure as well as P_1, it illustrates an important point concerning EOF analysis and the choice of variable. In choosing Brownian motion to model the zonal wind, we assumed a white vorticity field, constrained only to conserve angular momentum and satisfy the boundary conditions of the zonal wind. In EOF analysis of this vorticity field (not shown), all modes are almost degenerate, explaining nearly the same fraction of the variance. Integration to compute the zonal wind anomalies, M, separates modes with an n^{-2} spectrum, and the annular mode of the zonally averaged winds appears. A second integration to obtain the pressure, P_2, produces EOFs that decay as n^{-4}, further emphasizing the separation of scales.

While the atmospheric spectrum is not so extreme, there is a greater separation of scales with pressure (or geopotential height) than zonal winds. That the first EOF of pressure then explains a larger fraction of the variance is significant. Modes found in our simple models are more likely to be observed in the atmosphere if they are well separated, and thus more robust to rearrangement when the covariance structure is perturbed.

Why do these EOF patterns arise? Both the meridional dipole and annular zonal patterns are grave modes. In a field with a red spectrum, neighboring points are positively correlated. Hence, they will likely appear as the same sign in an EOF that will, by design, maximize the variance it can represent. Given this connection, EOF analysis simply links point to point, seeking to capture the entire domain in the first EOF. In the zonal direction this favors annular patterns. In the meridional, conservation of mass and zonal momentum provide an additional constraint; there must be at least

one node, and clearly, less pairwise variance is sacrificed with a single node than with two.

Zonal wavenumber-0 modes are expressions of rotational symmetry and meridional wavenumber-1 modes are expressions of mass and momentum conservation. It is therefore natural that such patterns are observed in simple dynamical models, full global climate models, and observations alike. This does not, of course, preclude the possibility that these patterns may be real dynamical modes. However, these are simply the patterns that one would expect to observe if the atmospheric velocity field were characterized by a random walk, subject to the constraints specified in (2.1). Thus, they provide a starting point for searching out the dynamically interesting side of extratropical low-frequency variability. Deviations from these patterns, for example, may suggest that other dynamics is occurring.

We draw the readers attention to related work by Wittman et al. (2005).

Acknowledgments. We thank Dr. Maarten Ambaum and two anonymous reviewers for helpful comments on an earlier draft. This work is supported by the Fannie and John Hertz Foundation and the NSF under Grant ATM-0337596.

APPENDIX

Stochastic Model Computations

a. Derivation of (2.10): The expected path of the Brownian bridge

We compute the expected, or average, path taken by all Brownian bridges with mean μ. For simplicity, we define this average path by the function $F(y, \mu)$:

$$F(y, \mu) \equiv E\left[B(\omega, y) \left| \int_0^1 B(y, \omega)\, dy = \mu \right. \right]. \quad \text{(A.1)}$$

Using the sinusoidal decomposition of B, Eq. (2.6), we have that

$$\int_0^1 B(\omega, y)\, dy = \frac{2\sqrt{2}}{\pi^2} \sum_{n=1,3,\ldots}^{\infty} \frac{1}{n^2} \zeta_n. \quad \text{(A.2)}$$

Equation (A.1) can then be written in terms of the ζ_n:

$$F(y, \mu) = E\left[\frac{\sqrt{2}}{\pi} \sum_{n=1}^{\infty} \frac{\zeta_n}{n} \sin(\pi n y) \left| \frac{2\sqrt{2}}{\pi^2} \sum_{n=1,3,\ldots}^{\infty} \frac{1}{n^2} \zeta_n = \mu \right. \right]$$

$$= \frac{\sqrt{2}}{\pi} \sum_{n=1}^{\infty} \frac{E[\zeta_n|\mu]}{n} \sin(\pi n y), \quad \text{(A.3)}$$

where $E[\zeta_n|\mu]$ is given by

$$E[\zeta_n|\mu] = E\left[\zeta_n \left| \frac{2\sqrt{2}}{\pi^2} \sum_{n=1,3,\ldots}^{\infty} \frac{1}{n^2} \zeta_n = \mu \right. \right]. \quad \text{(A.4)}$$

In the second step of (A.3) we have used the fact that, for random variables X and Y and scalars a and b, $E[aX + bY] = aE[X] + bE[Y]$, extended to the infinite sum.

We note that the condition on the mean of B only involves the odd ζ_n. As the ζ_n are independently distributed, knowledge about the values of the odd random variables provides no information about the even variables. Hence,

$$E[\zeta_n|\mu] = E[\zeta_n], \quad n = 2, 4, \ldots, \quad \text{(A.5)}$$

and $E[\zeta_n] = 0$, by construction.

For the odd terms, the problem is now to compute the expected value of each Gaussian variable, given the sum of them all. We use a result from probability theory: for independent, standard Gaussian variables X and Y and scalars a, b, and z:

$$E[X|aX + bY = z] = \frac{a}{a^2 + b^2} z. \quad \text{(A.6)}$$

Equation (A.6) can also be written as

$$E[aX|aX + bY = z] = \frac{a^2}{a^2 + b^2} z = \frac{\text{var}(aX)}{\text{var}(aX + bY)} z \quad \text{(A.7)}$$

so that the expected contribution of each variable to the sum is proportional to its variance. The result generalizes to an infinite sum of Gaussian variables, so that for n odd,

$$E[\zeta_n|\mu] = \frac{n^{-2}}{\sum_{m=1,3,\ldots}^{\infty} m^{-4}} \frac{\pi^2 \mu}{2\sqrt{2}} = \frac{24\sqrt{2}}{\pi^2} \frac{\mu}{n^2}, \quad \text{(A.8)}$$

where we use the sum

$$\sum_{m=1,3,\ldots}^{\infty} m^{-4} = \frac{\pi^4}{96}. \quad \text{(A.9)}$$

Inserting this result into (A.3) we conclude that

$$F(y, \mu) = \frac{48\mu}{\pi^3} \sum_{n=1,3,\ldots}^{\infty} \frac{1}{n^3} \sin(n\pi y) \quad \text{(A.10)}$$

$$= 6\mu \sum_{n=1,3,\ldots}^{\infty} \frac{8}{n^3 \pi^3} \sin(n\pi y) \quad \text{(A.11)}$$

$$= 6\mu y(1 - y), \quad \text{(A.12)}$$

where in the last step, we make use of the fact that on the interval [0, 1]

$$y(1 - y) = \sum_{n=1,3,\ldots}^{\infty} \frac{8}{n^3 \pi^3} \sin(n\pi y). \quad \text{(A.13)}$$

In passing, we note that $y(1 - y)$ is the variance of B so that its expected path, given the mean, is simply the variance function, suitably normalized. As observed when constructing the Brownian bridge, the expected path of a Wiener process, given its end point W(1), is $W(1)y$. The variance of $W(\omega, y)$ is also just y so that here, too, the expected path is given by the variance.

b. Derivation of (5.2): The expected path of the Wiener process

The expected path taken by a Wiener process, given its mean,

$$E\left[W(\omega, y) \,\middle|\, \int_0^1 W(\omega, y)\, dy = \mu \right] = \frac{3y}{2}\left(2 - y\right)\mu, \tag{A.14}$$

is computed by the same procedure used above. The Fourier decomposition of the Wiener process,

$$W(y) = \frac{\sqrt{2}}{\pi}\sum_{n=1}^{\infty}\frac{\zeta_n}{n}\sin[(n - 1/2)\pi y], \tag{A.15}$$

is used in place of the decomposition of the Brownian bridge, (2.6), and we make use of the result

$$\frac{3y}{2}(2 - y) = \sum_{n=1}^{\infty}\frac{6}{n^3\pi^3}\sin[(n - 1/2)\pi y] \tag{A.16}$$

on [0, 1]. There is no uncoupling between odd and even modes, as all basis functions have nonzero mean.

c. The Fourier decomposition of models P_1 and P_2

The Fourier decomposition of P_1 is

$$P_1(y) = \frac{\sqrt{2}}{\pi}\sum_{n=1}^{\infty}\left(\frac{\zeta_n}{n - 1/2} - \frac{6}{\pi^4(n - 1/2)^3}\sum_{m=1}^{\infty}\frac{\zeta_m}{(m - 1/2)^2}\right)\sin[(n - 1/2)\pi y]. \tag{A.17}$$

Model P_2 is obtained from M by integration of (2.11). The Fourier decomposition is

$$P_2(y) = \frac{f_0\sqrt{2}}{\pi^2}\sum_{n=1,3,\ldots}^{\infty}\left(\frac{\zeta_n}{n^2} - \frac{96}{n^4\pi^4}\sum_{m=1}^{\infty}\frac{\zeta_m}{m^2}\right)\cos(n\pi y) + \frac{f_0\sqrt{2}}{\pi^2}\sum_{n=2,4,\ldots}^{\infty}\frac{\zeta_n}{n^2}\cos(n\pi y). \tag{A.18}$$

REFERENCES

Ambaum, M. H. P., B. J. Hoskins, and D. B. Stephenson, 2001: Arctic oscillation or North Atlantic oscillation? *J. Climate,* **14,** 3495–3507; Corrigendum, **15,** 553.

Barnston, A. G., and R. E. Livezey, 1987: Classification, seasonality, and persistence of low-frequency atmospheric circulation patterns. *Mon. Wea. Rev.,* **115,** 1083–1126.

Batchelor, G. K., 1953: *The Theory of Homogeneous Turbulence.* Cambridge University Press, 197 pp.

Cash, B. A., P. Kushner, and G. K. Vallis, 2002: The structure and composition on the annular modes in an aquaplanet general circulation model. *J. Atmos. Sci.,* **59,** 3399–3414.

Feldstein, S. B., and S. Lee, 1998: Is the atmospheric zonal index driven by an eddy feedback? *J. Atmos. Sci.,* **55,** 3077–3086.

Kalnay, E., and Coauthors, 1996: The NCEP/NCAR 40-Year Reanalysis Project. *Bull. Amer. Meteor. Soc.,* **77,** 437–471.

Karatzas, I., and S. E. Shreve, 1991: *Brownian Motion and Stochastic Calculus.* Springer, 470 pp.

Knight, F. B., 1981: *Essentials of Brownian Motion and Diffusion*. American Mathematical Society, 201 pp.

Limpasuvan, V., and D. L. Hartmann, 2000: Wave-maintained annular modes of climate variability. *J. Climate,* **13,** 4414–4429.

Lorenz, D. J., and D. L. Hartmann, 2001: Eddy–zonal flow feedback in the Southern Hemisphere. *J. Atmos. Sci.,* **58,** 3312–3327.

North, G. R., and R. F. Cahalan, 1981: Predictability in a solvable stochastic climate model. *J. Atmos. Sci.,* **38,** 504–513.

——, T. L. Bell, R. F. Cahalan, and F. J. Moeng, 1982a: Sampling errors in the estimation of empirical orthogonal functions. *Mon. Wea. Rev.,* **110,** 699–706.

——, F. J. Moeng, T. L. Bell, and R. F. Cahalan, 1982b: The latitude dependence of the variance of zonally averaged quantities. *Mon. Wea. Rev.,* **110,** 319–326.

Obukhov, A. M., 1947: Statistically homogeneous fields on a sphere. *Usp. Mat. Nauk,* **2,** 196–198.

Thompson, D. W. J., and J. M. Wallace, 2000: Annular modes in the extratropical circulation. Part I: Month-to-month variability. *J. Climate,* **13,** 1000–1016.

Vallis, G. K., E. P. Gerber, P. J. Kushner, and B. A. Cash, 2004: A mechanism and simple dynamical model of the North Atlantic Oscillation and annular modes. *J. Atmos. Sci.,* **61,** 264–280.

von Storch, H., and F. W. Zwiers, 1999: *Statistical Analysis in Climate Research*. Cambridge University Press, 484 pp.

Wallace, J. M., 2000: North Atlantic Oscillation/Annular Mode: Two paradigms—One phenomenon. *Quart. J. Roy. Meteor. Soc.,* **126,** 791–805.

——, and D. S. Gutzler, 1981: Teleconnections in the geopotential height field during the Northern Hemisphere winter. *Mon. Wea. Rev.,* **109,** 784–812.

Wittman, M. A., A. J. Charlton, and L. M. Polvani, 2005: On the meridional structure of annular modes. *J. Climate,* **18,** 2119–2122.